

Revisiting the Membership, Multiplicity, and Age of the Beta Pictoris Moving Group in the *Gaia* Era

Rena A. Lee^{★1,2}, Eric Gaidos^{1,3,4}, Jennifer van Saders², Gregory A. Feiden⁵
and Jonathan Gagné^{6,7}

¹*Department of Earth Sciences, University of Hawai‘i at Mānoa, Honolulu, HI 96822, USA*

²*Institute for Astronomy, University of Hawai‘i at Mānoa, Honolulu, HI 96822 USA*

³*Institute for Astrophysics, University of Vienna, 1180 Wien, Austria*

⁴*Institute for Particle Physics & Astrophysics, ETH Zürich, 8093 Zürich, Switzerland*

⁵*Department of Physics and Astronomy, University of North Georgia, Dahlonega, GA 30597 USA*

⁶*Planétarium Rio Tinto Alcan, Espace pour la Vie, Montréal, Québec, Canada*

⁷*Institute for Research on Exoplanets, Université de Montréal, Montréal, Québec, Canada*

Submitted, accepted

ABSTRACT

Determining the precise ages of young (tens to a few hundred Myr) kinematic (“moving”) groups is important for placing star, protoplanetary disk, and planet observations on an evolutionary timeline. The nearby ~ 25 Myr-old β Pictoris Moving Group (BPMG) is an important benchmark for studying stars and planetary systems at the end of the primordial disk phase. *Gaia* DR3 astrometry and photometry, combined with ground-based observations and more sophisticated stellar models, permit a systematic re-evaluation of BPMG membership and age. We combined *Gaia* astrometry with previously published radial velocities to evaluate moving group membership in a Bayesian framework. To minimize the effect of unresolved stellar multiplicity on age estimates, we identified and excluded multi-star systems using *Gaia* astrometry, ground-based adaptive optics imaging, and multi-epoch radial velocities, as well as literature identifications. We estimated age using isochrone and lithium-depletion-boundary fitting with models that account for the effect of magnetic activity and spots on young, rapidly rotating stars. We find that age estimates are highly model-dependent; Dartmouth magnetic models with ages of 23 ± 8 Myr and 33^{+9}_{-11} Myr provide best fits to the lithium depletion boundary and *Gaia* M_G vs. $B_P - R_P$ color-magnitude diagram, respectively, whereas a Dartmouth standard model with an age of 11^{+4}_{-3} Myr provides a best fit to the 2MASS-*Gaia* M_{K_S} vs. $B_P - R_P$ color-magnitude diagram.

Key words: stars: evolution – binaries: general – Hertzsprung-Russell and colour-magnitude diagrams – stars: low-mass – stars: pre-main-sequence

1 INTRODUCTION

Associations of nearby, kinematically coherent, coeval stars, known as young moving groups (YMGs), are indispensable laboratories for studying early stellar and planetary evolution. Studies of YMG members have informed research on early evolution of stellar interiors, rotation, magnetic activity, and high-energy emission (Kastner & Principe 2022), protoplanetary disk-dissipation timescales (Silverberg et al. 2020; Higashio et al. 2022), and the occurrence of giant planets (Nielsen et al. 2019). Accurately describing these evolutionary sequences relies on precise and accurate ages for these groups, i.e., by fitting model isochrones to stars in a color-magnitude diagram, modeling the depletion of lithium in the lowest-mass members, or back-tracking stars to a common spatial origin based on their

kinematics. The ages of individual members (and their planets) can then be assigned to the ensemble age of the host YMG¹. In recent years, the advent of all-sky photometric and astrometric surveys, especially by the *Gaia* mission, has enabled the identification of new members of known YMGs, as well as discovery of new groups (Faherty et al. 2018; Gagné & Faherty 2018; Ujjwal et al. 2020; Lee et al. 2022).

The β Pictoris Moving Group (BPMG), as the youngest, nearest (median distance ~ 50 pc) YMG, permits some of the most detailed studies of pre-main sequence stars (pre-MS), including the intrinsically faintest (lowest and substellar-mass) members. Projected angular separations between binaries are larger, facilitating

¹ This assumes star formation occurred over an interval that is short compared to the age of the group.

★ Contact e-mail: renaalee@hawaii.edu

the identification and characterization of stellar and substellar companions to the members. The age of the group, estimated to be ~ 25 Myr by lithium depletion boundary (LDB) fitting (Messina et al. 2016), isochrone fitting, and dynamical traceback (Mamajek & Bell 2014), corresponds to an epoch immediately following the dissipation of protoplanetary disks and the initial phase in the evolution of fully-formed stars and planets. The BPMG’s eponymous star, β Pictoris, hosts one of the first directly imaged debris disks (Lecavelier Des Etangs et al. 1993), as well as a rare directly imaged multi-planet system (Lagrange et al. 2020). Among other BPMG members are 51 Eridani, hosting a directly imaged Jupiter analog (Macintosh et al. 2015), PSO J318.5-22, a free-floating planet (Liu et al. 2013), and AU Microscopii, hosting an edge-on debris disk and two transiting planets (Kalas et al. 2004; Plavchan et al. 2020; Cale et al. 2021).

The age of the BPMG has been estimated by fitting model isochrones to sequences in color-magnitude diagrams (CMDs), dynamical traceback analyses, and lithium-depletion-boundary (LDB) model fitting. The derived values range between 10 and 50 Myr, with considerable variation in the uncertainties (Fig. 1, Mamajek & Bell 2014). The most recent estimates cluster around 20-25 Myr, placing the BPMG at an intermediate stage between the Upper Scorpius star-forming region (10 ± 3 Myr, Pecaute & Mamajek 2016), and the Carina YMG at 38-56 Myr (Bell et al. 2015; Gaidos et al. 2022). Dynamical traceback studies of BPMG kinematics suggest a single star-forming origin (e.g., Crundall et al. 2019; Miret-Roig et al. 2020), and thus is no evidence for a physical age spread among BPMG members.

Several effects can contribute to systematic error in the estimated ages of moving-groups. Contamination by non-members from the field can increase the scatter in color-magnitude diagrams and cause a group to appear older. Stars in other, older moving groups within the solar neighborhood, which are more likely to have space velocities more similar to BPMG, may also erroneously be identified as members. Non-members contaminating the sample can be identified and removed based on Galactic space motions, but this requires precise parallaxes, proper motions, and radial velocities (RVs). Unresolved binary companions can make members appear more luminous and hence younger than they actually are on CMDs (Sullivan & Kraus 2021), affect the kinematics used for trace-back analysis, or influence the depletion of Li through the effect of a stellar companion on disk dissipation and stellar rotation (Somers & Pinsonneault 2015). Previous studies have highlighted the importance of identifying and excluding binary systems from group age analyses (e.g., Binks & Jeffries 2014; Alonso-Floriano et al. 2015; Messina et al. 2017). Recently, Miret-Roig et al. (2020) used *Gaia* DR2 astrometry and ground-based RVs to assess the BPMG age, identifying binaries based on the astrometry and RV variability.

An additional source of uncertainty in deriving ages from model comparisons comes from the elevated activity of members of young groups. At young (< 0.5 Gyr) ages, most low-mass ($< 0.8 M_{\odot}$) stars are rapidly rotating ($P < 10$ d), and the surface spottedness and magnetic activity of pre-MS stars are observed to be enhanced compared to more quiescent MS stars (Morris 2020). It is not known if any observed internal age gradients within stellar groups are physical, as the mass-dependence of star formation timescales is not well established. Multiple epochs of star formation may contribute to actual scatter in group age estimates (Krumholz et al. 2019), but as mentioned, this case has not been supported by dynamical studies of BPMG (Crundall et al. 2019; Miret-Roig et al. 2020).

An individual star’s membership in a YMG is typically as-

sessed by comparing its position in Galactic 6-d (3-d position and 3-d space velocity) phase space to that of the established group mean and dispersion. Previous BPMG membership studies have cataloged candidate members (e.g., Gagné & Faherty 2018) using incomplete astrometric (5-D; 3-D position and 2-D motion) information, followed by measurement of the 6th (RV) dimension to confirm membership (e.g., Schneider et al. 2019). Additionally, several studies have used RVs to identify binaries among BPMG members (Alonso-Floriano et al. 2015; Messina et al. 2017; Miret-Roig et al. 2020). However, multi-epoch observations were often not available, meaning that single-lined spectroscopic binaries with variable RVs could not be identified.

The advent of the *Gaia* mission (Gaia Collaboration et al. 2016) has provided the precise astrometry and, for many sufficiently bright stars, RVs, to calculate space motions and vet members of YMG. Incomplete RV information can be complemented by ground-based surveys such as the Radial Velocity Experiment (RAVE, Steinmetz et al. 2020). *Gaia* also provides precise and homogeneous optical photometry, i.e. magnitudes in the *G*-band (similar to but much wider than Cousins *R*) and a $B_p - R_p$ color constructed from its wavelength-dispersing photometer. These can be used to construct color-magnitude diagrams to compare with model isochrones, and to identify unresolved binaries or contaminated single-star sources via over-luminosity relative to known single stars. *Gaia* Data Release 3 provides a metric of astrometric error, the Reduced Unit Weight Error (RUWE), relative to a single-star solution, that can be used to identify unresolved binaries (Belokurov et al. 2020; Wood et al. 2021). This can be complemented by high-angular resolution adaptive optics (AO) imaging obtained by searches for substellar companions; these can readily detect stellar companions at separations of ~ 10 -1000 au.

New, diverse evolutionary models are available to compare with photometry and measurements of Li abundance, in particular those addressing the effects of magnetic activity and starspots on the structure, convection, and luminosity of low-mass pre-MS stars (Feiden 2016; Somers et al. 2020). The contribution of magnetic pressure to the internal gas equation of state and total near-surface pressure leads to inflated predicted radii for a given mass and age relative to non-magnetic models, or, for a given luminosity and effective temperature, to an older model age.

In this work, we combined precision astrometry, photometry, and RVs from *Gaia* DR3 with ground-based RV measurements and AO imaging to assess and confirm moving group membership, identify and exclude close binaries, and distill a catalog of single-star members of the BPMG suitable for age analysis by the CMD and LDB methods. Further, we compared our estimate of the multiplicity fraction from this work with those of other young stellar associations. We fit predictions from a suite of evolutionary models designed for spotted, magnetically active stars to precise, homogeneous measurements of these stars to revisit the age of the BPMG, and consider the implications of our new, model-dependent ages.

2 OBSERVATIONS AND METHODS

2.1 Catalog Construction

We obtained confirmed and candidate members of the BPMG from the Gagné et al. (2018) catalog, which analyzed all *Gaia* DR2 sources with precise parallaxes within the nearest 100 pc for YMG membership. We screened additional confirmed and candidate members from Binks & Jeffries (2014), Binks & Jeffries (2016),

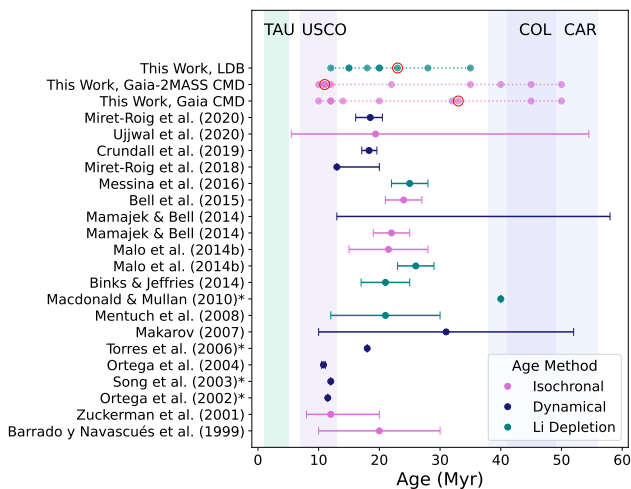


Figure 1. Estimates of the age of the BPMG in the literature, i.e. Table 6 of Miret-Roig et al. (2020), updated from Table 1 of Mamajek & Bell (2014), along with the CMD- and LDB-based ages from this study. The best-fit ages for each of three methods used in this work are circled in red. Estimated ages of other young stellar associations Taurus (TAU), Upper Scorpius (USCO), Carina (CAR), and Columba (COL) from Table 1 in Gagné & Faherty (2018) have been plotted for comparison and context. The sources for ages marked with a "*" do not report errors for their ages.

Kiss et al. (2011), Lee & Song (2018), Messina et al. (2017), and Shkolnik et al. (2017), yielding an initial catalog of 433 (assumed individual) stars. Binaries are discussed in Sec. 2.2. This sample was cross-matched with *Gaia* DR3 (Gaia Collaboration et al. 2021) and astrometry and photometry were incorporated for 415 stars and RVs for 99 stars. In total, RVs of 238 candidates were gathered, from RAVE DR6 (Guiglion et al. 2020), and previous RV surveys of low-mass stars and YMGs (i.e., Binks & Jeffries 2016; Malo et al. 2014a; Shkolnik et al. 2017; Terrien et al. 2015), in addition to the *Gaia* RVs.

We calculated probabilities of BPMG membership using BANYAN Σ , a multivariate Bayesian classifier (Gagné et al. 2018). BANYAN Σ calculates UVW space velocities and XYZ galactic positions from coordinates, proper motions, parallaxes, RVs, and their errors, and compares these to the six-dimensional group means and standard deviations of the 27 nearest identified young moving groups. For candidates with multi-epoch RV measurements, we used the median values in the BANYAN inputs. For candidates with an even number of epochs, the mean of the median values were used. Based on the distribution of membership probabilities computed for candidates with complete kinematic data, we chose a threshold probability of 0.9; this selected 148 of 238 candidates with RV measurements. Separately, we identified 63 of the 195 candidates lacking RVs which would have membership probabilities >0.9 for an "optimal" RV that maximizes that probability and is plausible, i.e., is within the distribution of the measured RVs of confirmed members. These are high-priority targets for ongoing RV follow-up but are not further analyzed in this work.

Main sequence stars could be interlopers if their space motions coincide by chance with the BPMG. To identify and filter these, we compared $p > 0.9$ candidates with the empirical main sequence of Pecaut & Mamajek (2013) in a absolute G magnitude vs. $B_p - R_p$ color CMD (Fig. 2). We computed the minimum offset in G magnitude of each candidate from the MS. Based on the distribution

of offsets, we chose a cutoff of 0.55 mags and removed nine stars within 0.55 mags of the MS locus and $B_p - R_p > 2$, corresponding to a mass of $< 0.55 M_\odot$ (Pecaut & Mamajek 2013), as interlopers. We retained stars with $B_p - R_p < 2$ since hotter, more massive stars can be close to or on the MS by the age of the BPMG (Krumholz et al. 2019).

We cross-matched BPMG stars with the 2-Micron All-Sky Survey (2MASS) Point Source Catalog (Skrutskie et al. 2006) to obtain JHK_s -band photometry in the infrared, and we corrected for extinction and reddening based on the Leike et al. (2020) 3-d ISM dust distribution using Dustmaps (Green 2018). As expected for nearby stars, ISM reddening is small; the mean reddening is $E(B - V) = 0.0005$ mag, and the mean extinction values are $A_G = 0.0003$ mag and $A_{K_s} = 7.1 \times 10^{-5}$ mag.

The 4" resolution of the 2MASS survey means that many binary stars will be unresolved. Unresolved or partially resolved sources can lead to erroneously brighter and somewhat redder photometry that in turn can affect age-dating (Sullivan & Kraus 2021). To minimize this systematic, we corrected the K_s -band photometry of those binaries that were resolved by *Gaia* (see Section 2.2) but not resolved by 2MASS (noted in Table 2). We predicted the 2MASS K_s magnitude of each *Gaia*-resolved component using the G magnitude of each component and a relation between $G - K_s$ and $B_p - R_p$ based on the empirical main sequence of Mamajek & Bell (2014)². We then compared the predicted and the measured K_s mags, and based on the overall distribution of the differences, we flagged systems with a difference >0.25 mag as significantly contaminated by a companion. Based on the contrast of the predicted K_s magnitudes, we apportioned the measured K_s -band fluxes between the binary components, and apparent K_s mags from those fluxes. This salvaged 9 systems for use in the K_s vs. $B_p - R_p$ CMD fitting in Sec. 3.1.

2.2 Binary Identification

We retrieved visual and spectroscopic binary systems from Shkolnik et al. (2017) and spectroscopic and RV binary systems from Miret-Roig et al. (2020). We identified additional binary/multiple systems that appear as *Gaia*-resolved components in the DR3 astrometric catalog, unresolved systems identified by *Gaia* astrometric error, systems that are resolved in high-resolution AO imaging, and unresolved systems via multi-epoch RV variability or over-luminosity relative to the single-star locus in a CMD. Fig. 3 shows the approximate coverage of these different methods in magnitude contrast-separation space.

Gaia resolved binaries: We identified sources within 30" with similar parallaxes and proper motions; this search radius corresponds to a binary separation of 1500 au at the median distance of BPMG members, well beyond the peak of the M dwarf binary separation distribution at 50 au (Susemihl & Meyer 2022), or ~ 5 au (Winters et al. 2019), and thus encompassing the vast majority of physical companions. For each pair of member and potential companion we computed likelihoods P_1 and P_2 that the latter is a common proper-motion companion or an interloper from the field, respectively. We then compute a Bayesian probability $P_c/(P_c + P_f)$,

² This color-color relation is based on main sequence stars and ignores metallicity effects but should be approximately correct for BPMG members.

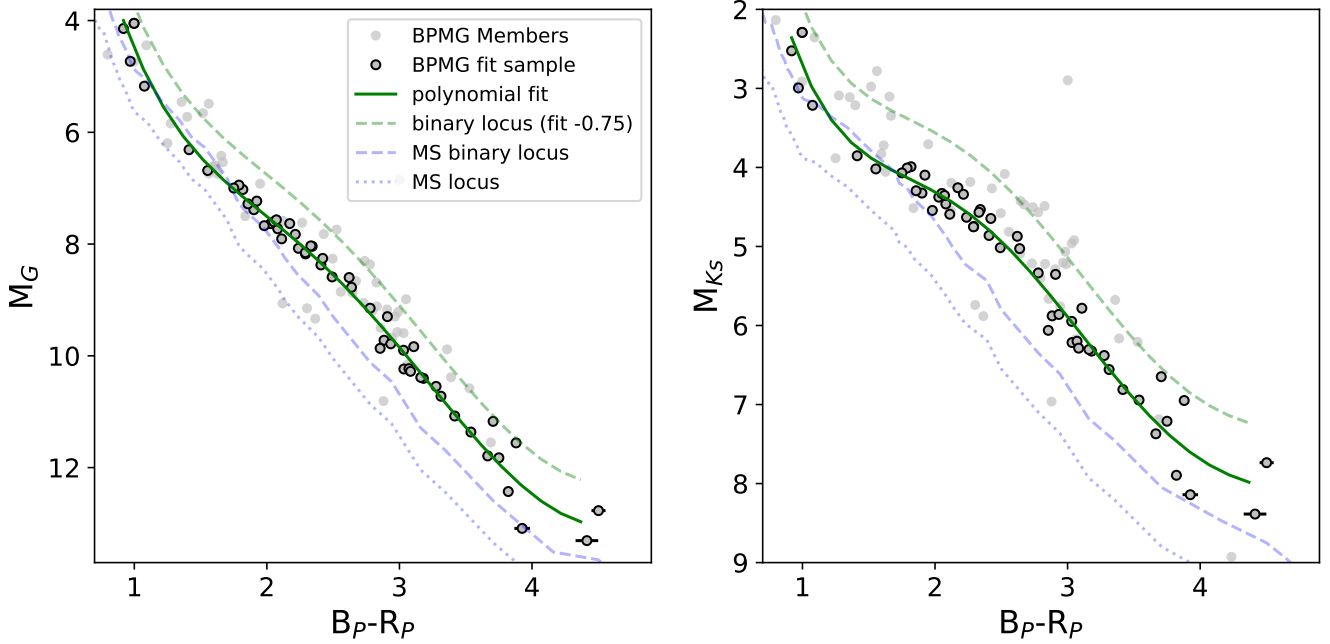


Figure 2. *left:* Color-magnitude diagram (CMD) based on *Gaia* absolute G magnitudes and $B_P - R_P$ colors of confirmed BPMG members. *right:* CMD using absolute 2MASS K_s magnitude in place of M_G . All confirmed BPMG members are shown as grey dots, while those passing the binary exclusion and photometric criteria and used for age estimation (outlined in black) are used in the isochrone fitting described in Sec. 3.1. The solid green lines are the best-fit lines in each diagram (5th degree polynomial) and the dashed green lines are the equal-mass binary loci (displaced by $-2.5 \log 2 \approx -0.75$ mag from the best-fit loci). The blue dashed line is the equal-mass binary locus constructed from the empirical main sequence (blue dotted line) of Pecaut & Mamajek (2013).

where $P_{c,f}$ are both evaluated as:

$$P = \sum_i \Delta\mu_i \times \exp\left(-\frac{\Delta\mu_i^2}{2} \frac{1}{\sigma_\mu^2 + \mu_{\text{orb}}^2} - \frac{\Delta\pi^2}{2\sigma_\pi^2}\right) \frac{1}{\sigma_\mu^2 + \mu_{\text{orb}}^2} \frac{1}{\sigma_\pi}, \quad (1)$$

except that while the sum for P_c consists only of a contribution from a single putative companion, the sum for P_f is over all stars from an equivalent search at an uncorrelated (distant) location from the BPMG member. In Eqn. 1, $\Delta\pi_i$ and $\Delta\mu_i$ are the difference in parallax and proper motion, respectively, σ_π and σ_μ are the standard errors in parallax and proper motion of a stellar pair, added in quadrature, and μ_{orb} is the typical proper motion due to orbital motion, included as a “softening” term. This was estimated by considering the peak separation of nearby (< 25 pc) M dwarf binaries, 5 au (Winters et al. 2019), and $2\pi \cdot 5 \approx 30$ au orbit. For missions such as *Gaia*, a five-year baseline would allow detection of ~ 6 au yr^{-1} orbital motion, which at the BPMG’s median distance of 50 pc, is on the order of 100 mas yr^{-1} . Because of orbital inclinations and eccentricities, realistically there would be a decrement in the observed orbital motions on the order of a half. For our computations, we adopted $\mu_{\text{orb}} = 10$ mas yr^{-1} , which follows from an orbital motion of ~ 0.5 au yr^{-1} . Wider separations would correspond to smaller orbital motions that are not detectable.

Based on the distribution of P values we adopted a cutoff of $P > 0.98$. Our Bayesian analysis identified 30 likely multi-star systems; 29 binaries and one triple. We confirmed 14 of these companions as BPMG members based on their astrometry, independent RVs, and BANYAN Σ . The separations and magnitude contrasts of these 14 systems are shown in Fig. 3 as purple squares, labeled “*Gaia* Resolved.” Binary systems resolved by *Gaia* and 2MASS were included in subsequent analyses; those resolved by *Gaia* but

not by 2MASS were included if the latter were resolved with AO imaging (see below) or corrected for source confusion as described above.

AO imaging: We collected archival AO images of confirmed BPMG members obtained with any of three instruments: NAOS+CONICA (NACO) on the ESO VLT UT1 (Lenzen et al. 2003; Rousset et al. 2003), NIRC2 on Keck-2 (Service et al. 2016), and NIRI on Gemini-North (Hodapp et al. 2003) from the ESO, Keck Observatory, and Gemini Observatory archives, respectively. In each archive, we performed a $10''$ cone search (the typical field of view) of the coordinates of each member. We retrieved at least one AO image for 117 BPMG members, and we inspected each image for additional sources. In Fig. 3 (left) we plot the 16 AO-resolved binary components as pink triangles. An injection-and-recovery analysis was performed to assess the completeness and false positive rate of our visual inspection, i.e. by adding simulated companions to randomly selected AO images containing a single (real) star. The point spread function of the target star was scaled and used for the simulated (mock) companion. The magnitude contrast of the simulated companion was randomly sampled from a uniform distribution in magnitude, and the separation was sampled from the Winters et al. (2019) orbital distribution of nearby M dwarf systems, assuming a distance of 50 pc. Separations were limited to $1.5''$ to focus on a region of the parameter space not resolved by *Gaia*; the recovery and false-positive rates at wider separations is expected to be the same as at $1.5''$ out to at least $\sim 5''$, half the field of view of the NIRC2 images. The results of the data injection recovery are shown in Fig. 3 (right). We performed a kernel density estimation using the Python package `sklearn.neighbors.KernelDensity` (Pedregosa et al. 2011) on the recovered (green points) and not-recovered (open points) simulated companions to establish a 50%

detection efficiency contour in separation-magnitude contrast space (Fig. 3 (right)). From the injection-and-recovery analysis, we found the visual inspection was reliable for detecting companions having up to 4.5 magnitudes of contrast with the primary and separation as small as 40 mas.

Gaia astrometric error: *Gaia* RUWE is a measure of astrometric error relative to a single-star fit that is analogous to reduced χ^2 . Stars with RUWE > 1.4 are almost invariably unresolved binaries (A. Kraus, pers. comm., Belokurov et al. 2020). Fitton et al. (2022) found that single stars hosting protoplanetary disks also exhibit elevated RUWE, but BPMG members are known to host only much less substantial debris disks (Lagrange et al. 2010). Twenty-nine members were identified as *Gaia*-unresolved binaries based on RUWE.

Radial velocities: Sources with ground-based RVs at more than one epoch were assessed for binarity based on a reduced χ^2 test. Based on the distribution of values, we chose a criterion of $\chi^2_V > 20$, flagging 6 systems. We show in Fig. 3 an estimated RV detection limit contour based on the separations and magnitude contrast of the resolved BPMG binaries and the average RV amplitude from members with multi-epoch RVs. We computed the expected separation and magnitude contrast of unresolved binary systems assuming a typical primary mass of $0.3 M_\odot$ (for M dwarfs) and maximum separation of 1000 au. Additionally, the probability of the null hypothesis (p -value) for RV variability are included for many sufficiently bright stars in *Gaia* DR3 (Chance et al. 2022) and 14 sources for which $p < 0.01$ were flagged as spectroscopic binaries.

Photometry: Additional candidate binaries were identified by the over-luminosity of stars with respect to the nominal single-star locus for BPMG (described in Sec. 2.1). We assumed the stars to be equal-brightness, the most probable configuration among M dwarfs (Duchêne & Kraus 2013) and constructed a binary locus for the BPMG by shifting the single-star locus by -0.75 mag. We quantified the absolute offset in M_G , ΔM_G , of individuals from this locus and identified 18 likely photometric binaries based on a cut-off of $\Delta M_G < 0.7$ mag.

In summary, our membership catalog began with 433 candidate sources compiled from the literature, of which 238 were tested for BPMG membership with full kinematic data. Among the 148 confirmed members, we identified 30 resolved binary systems; 14 from the *Gaia* proper motion matching and 16 from AO imaging. We identified and excluded 61 unresolved binary systems from subsequent analyses; 29 from *Gaia* RUWE, 14 from RVs, and 18 from photometry. Since they are not resolved, they are not shown in Fig. 3 (left), though we provide approximate detection limits for these methods. This left 64 single stars and 30 resolved binary systems for subsequent analyses.

3 AGE DETERMINATION

3.1 Isochrone Fitting

We estimated the age of the BPMG by fitting isochrones from different model suites to the confirmed members that are single or resolved binaries in the two CMDs plotted in Fig. 2. We assessed four combinations of *Gaia* and 2MASS colors and magnitudes: M_G vs. $B_P - R_P$, M_{K_s} vs. $B_P - R_P$, M_G vs. G-K, and M_{K_s} vs. G-K. To quantify the scatter in each locus, we computed the χ^2 offsets from best-fit 5th order polynomials for each CMD. The final sample for isochrone fitting is plotted in M_G vs. $B_P - R_P$ and M_{K_s} vs. $B_P - R_P$ CMDs (Fig. 2), which are the two best-performing choices of color-magnitude pairs for CMD analysis. We used the pre-MS models of

Baraffe et al. (2015), the Dartmouth standard and magnetic models (Feiden 2016), and the SPOTS models of Somers et al. (2020). The Baraffe et al. (2015) models (hereafter, BHAC) are calibrated for pre-MS and MS low-mass stars. The evolutionary calculations are based on standard input physics of stellar interiors (Chabrier & Baraffe 1997), but with updated atmosphere models compared to the predecessor evolutionary models of Baraffe et al. (1998). While the BHAC models are calibrated for pre-MS stars, they do not account for the effects of stronger magnetic fields occurring at the surfaces of young, rapidly rotating stars. We interpolated model values of *Gaia* and 2MASS magnitudes over the provided masses and ages to produce a finer age model grid (spaced by 1 Myr) than is provided in Baraffe et al. (2015) to better intercompare the precise colors and absolute magnitudes.

Dartmouth stellar evolution models are suitable for modeling low-mass main sequence (Dotter et al. 2008) and pre-MS stars (Feiden 2016), with or without the effects of stellar magnetic fields (Feiden & Chaboyer 2012; Feiden 2016). The magnetic and non-magnetic models were used to age-date BPMG in Malo et al. (2014b). Their interior structure and evolution calculations adopt standard input physics (e.g., solar-calibrated mixing length, general ideal gas equation-of-state, and MARCS (Gustafsson et al. 2008) model atmospheres) comparable to other modern low-mass stellar models (e.g., BHAC; Dotter et al. 2008), with updates to improve the accuracy of model predictions for very-low-mass stars and the pre-main-sequence phase of stellar evolution (e.g., Malo et al. 2014b; Feiden et al. 2015). Models including magnetic fields account for the impact of magnetism on the gas equation of state and on the efficiency of thermal convection (Feiden & Chaboyer 2012; Feiden 2016). Surface magnetic field strengths are assumed to be in pressure equipartition with the gas near the stellar photosphere (Feiden 2016). The model grid assumes solar metallicity (appropriate for the BPMG) and solar composition (Grevesse et al. 2007) and includes individual mass tracks with $0.1 \leq M/M_\odot \leq 2.0$, and isochrones with ages from 1 Myr – 10 Gyr. Synthetic *Gaia* photometry is calculated using synthetic spectra from MARCS model atmospheres (Gustafsson et al. 2008), 2MASS *JHK_s* passbands (Skrutskie et al. 2006), and revised *Gaia* DR2 passbands (Evans et al. 2018) assuming the extinction A_V is zero.

SPOTS evolutionary models (Somers et al. 2020) address the distorting effects of activity and surface spots on the structure of magnetically active stars. The model grid includes evolution tracks and isochrones for $0.1 - 1.3 M_\odot$ stars with discrete surface spot coverage fractions of $f = 0.0, 0.17, 0.34, 0.51, 0.68, \text{ and } 0.85$. The SPOTS isochrones are empirically calibrated from the color transformations of Pecaute & Mamajek (2013). However, *Gaia* magnitudes and colors are not provided for objects redder than $B_P - R_P \sim 2.5$ for models and $f > 0$, where many BPMG members lie. We extend the fits to $B_P - R_P = 3$ for $f > 0$ cases using the model luminosity, gravity, mass, and dual-temperature regime (for hot and cool surface regions) to obtain bolometric corrections (and hence absolute magnitudes) for *Gaia* G , B_P , and R_P and 2MASS K_s magnitudes from the YBC database of bolometric corrections (Chen et al. 2019), assuming $A_V=0$ and solar metallicity. The $B_P - R_P$ colors were generated by taking the difference between the absolute B_P and R_P magnitudes.

We computed the spot fractions f , which are specified in terms of surface area, to fractions in luminosity f' using:

$$f' = \frac{f}{f + (1 - f)(T_{\text{hot}}/T_{\text{cool}})^4}. \quad (2)$$

The two model temperatures, T_{hot} and T_{cool} from SPOTS were used

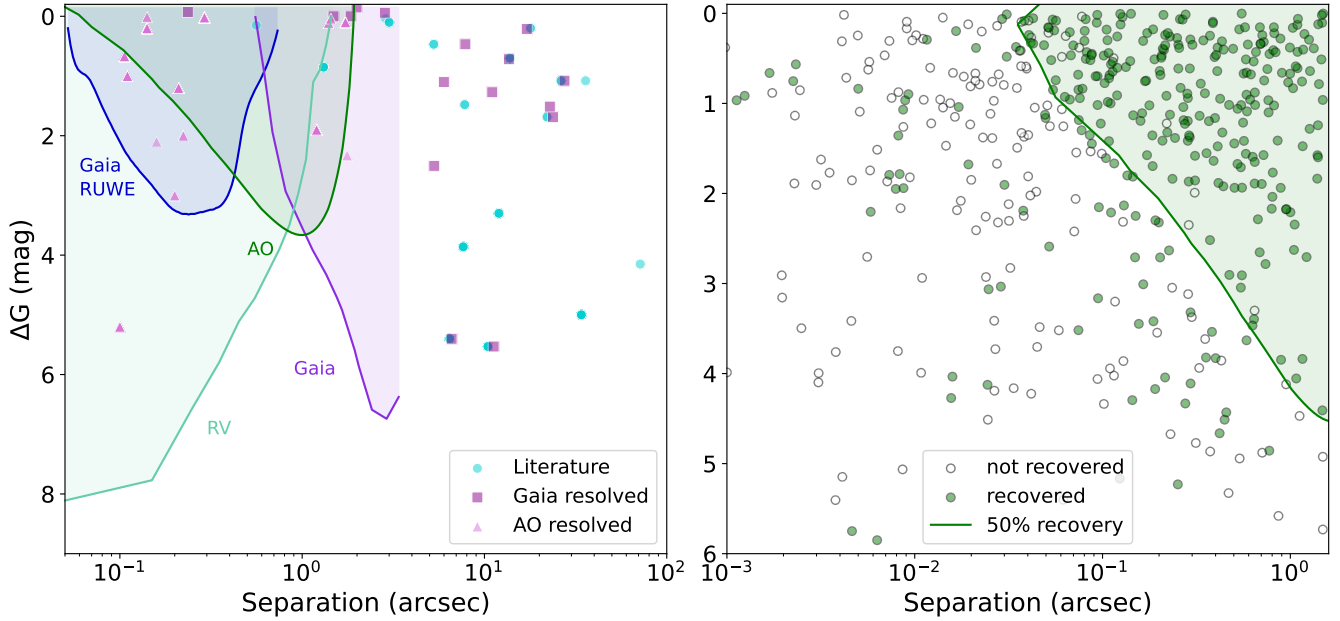


Figure 3. *Left:* Separation vs. magnitude contrast for binary components in the BPMG primary sample from the present *Gaia* cone search astrometry comparison and AO image inspection, as well as literature-reported binaries. Unresolved photometric, spectroscopic, and RUWE-identified binaries are not included since these parameters cannot be unambiguously determined. Also plotted are 50% recovery contours for *Gaia* RUWE binaries from Wood et al. (2021), *Gaia*-resolved binaries from Ziegler et al. (2018) and for AO from our injection-and-recovery tests. The estimated RV detection limit, based on an assumed primary mass of $1 M_{\odot}$ and average RV amplitude of 20 km s^{-1} , is shown in light green. *Right:* Results of the AO injection-and-recovery analysis. Simulated binaries that were not recovered by eye (false negatives) are plotted as open points, and successful recoveries are plotted as filled points. The contour represents a 50% detection efficiency.

to separately compute magnitudes and relative fluxes for hot and cool surface regions, and an average flux was computed based on our modified spot fractions. Objects redder than $B_P - R_P = 3$ are still included in the fits.

To fit isochrones we used the τ^2 metric (Naylor & Jeffries 2006), a form of 2-D maximum-likelihood fitting. τ^2 behaves essentially as a χ^2 statistic, with an added dependence on the model density of stars in color-magnitude space (ρ in Eqn. 5 of Naylor & Jeffries 2006). We show in Fig. 4 the results of our isochrone fitting analysis for each of the nine models (BHAC, Dartmouth standard, Dartmouth magnetic, and SPOTS models for each of six values of spot fraction), in *Gaia* $B_P - R_P$ vs. M_G and M_{K_S} CMDs. To better visualize the details of model performance, the difference in absolute magnitude vs. $B_P - R_P$ for each model relative to the 5th degree polynomial fits to the main BPMG locus are plotted in Fig. 4. (See Fig. 2 for an uncluttered look at the sample and polynomial fits). We report the best-fit ages and τ^2 values from each of the fits in Table 1.

3.2 Lithium Depletion Boundary Analysis

We compared observed and model abundance of lithium vs. effective temperature as an independent constraint on the age of the BPMG. Measurements of the equivalent width (EW) as well as upper limits for the strength of the Li I doublet at 6708 \AA were gathered from the literature (Bowler et al. 2019; Mentuch et al. 2008; Messina et al. 2016; Zuckerman et al. 2001) for single BPMG members. For this analysis, we chose to exclude binary systems due to confusion in deriving accurate abundances for each binary component, as well as the potential effect of a companion on rotational spin-down

and Li depletion timescales compared to single stars (Somers & Pinsonneault 2015; Bouvier et al. 2018). EWs were converted to normalized abundances based on the curves of growth of Palla et al. (2007) in the T_{eff} range 3100–3600 K and Soderblom et al. (1993) in the T_{eff} range 4000–6500 K. We scaled these normalized abundances to absolute values assuming $A(\text{Li}) = 3.30$ dex on an $A(\text{H})=12$ scale, a value based on meteoritic abundances, a proxy for Li in the protosolar value (Asplund et al. 2009). A typical abundance uncertainty was computed from the typical EW error and T_{eff} error added in quadrature. We show the converted Li abundances as a function of *Gaia* $B_P - R_P$, a proxy for T_{eff} , in Fig. 6, along with predicted abundances from each of the nine models. For each of the models, we identified the best-fit models by minimum χ^2 fit.

4 RESULTS

4.1 Membership and Multiplicity

From an initial list of 238 stars with complete kinematic information we identified 148 as members of BPMG with a Bayesian probability $P > 0.9$. Fifteen members were already identified in the literature as binaries. 30 systems were identified as resolved binary systems in *Gaia* DR3 and of these, 14 new companions were independently confirmed in BANYAN. 16 binary companions were resolved in AO images; 4 of which were identified in the *Gaia* search. Table 2 catalogs confirmed BPMG members in 132 systems, including 64 single stars, 42 resolved binaries, and 47 unresolved binaries. Members of binary systems and those for which the 2MASS K_s magnitudes were recomputed based on *Gaia* photometry are flagged in Table 2.

We found that 38–51% of BPMG systems are binaries, the

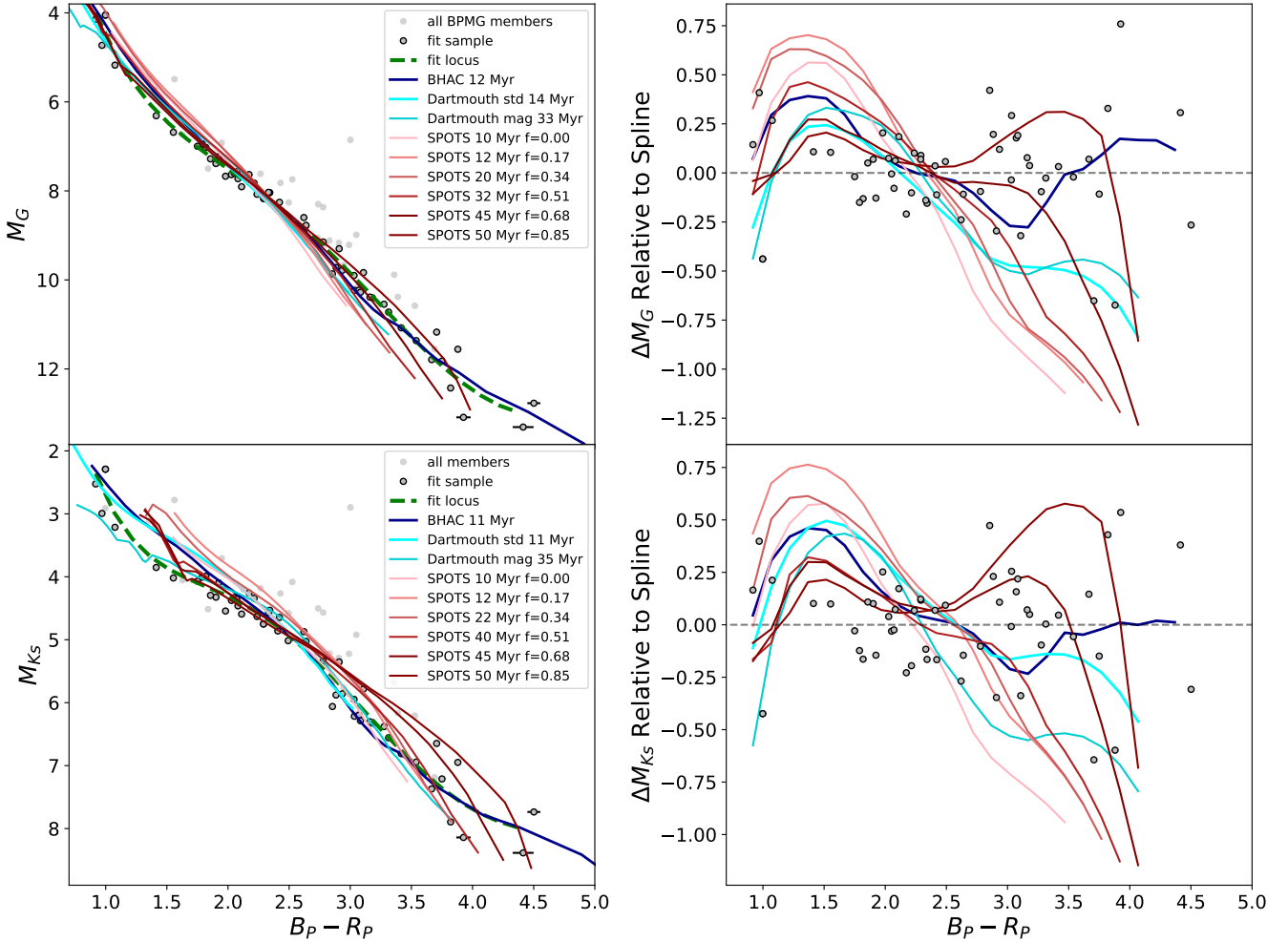


Figure 4. *Gaia* (top) and 2MASS-*Gaia* (bottom) color-magnitude diagrams of the single star BPMG sample. All BPMG members confirmed in this study are shown as grey dots, while those passing the binary exclusion and photometric criteria are outlined in black. Only those outlined are used in the isochrone fitting. *Left:* Best-fit isochrones by minimum τ^2 . For the SPOTS isochrones, f' denotes the revised spot fraction (Eq. 1) from YBC corrections. In both panels, we show a best-fit spline to the main BPMG locus in red. *Right:* Each of the nine best-fit isochrone curves relative to the spline fit to better visualize the regions of the CMD where the models tend to fit or fail. The τ^2 values for each fit are given in Table 1.

proportion of binary to single systems in this sample, consistent with previous estimates for pre-MS stars in the literature ($\sim 50\text{--}58\%$, Ghez et al. (1997)). The upper bound of the multiplicity fraction assumes the AO-resolved systems within 4" are bound, as is supported statistically (Kraus & Hillenbrand 2008). We also include all over-luminous sources (candidate binaries identified by photometry) in this estimate, as a majority of them were additionally suggested to be binaries by *Gaia* RUWE or proper motion matching. Excluding these systems would yield a conservative multiplicity lower-limit of 38%. We compare our results to other YMGs and the field in Fig. 5, adapted from Shan et al. (2017) and updated with Jaehnig et al. (2017); Kounkel et al. (2019); Zúñiga-Fernández et al. (2021), with age estimates based on BANYAN (Gagné et al. 2018) and SACY (Search for associations containing young stars; Zúñiga-Fernández et al. 2020) membership catalogs. The binary fraction in 1–50 Myr clusters and groups other than BPMG appear to have relatively lower binary fractions (Jaehnig et al. 2017; Shan et al. 2017; Zúñiga-Fernández et al. 2021). This is possibly because

the binary analysis in this work was more thorough than those of those other, more distant groups and clusters.

4.2 Age Estimates

For our age analysis, we excluded 47 confirmed members systems due to unresolved binarity; 29 of these were based on the *Gaia* RUWE criterion, 21 based on RV variability, and 18 based on photometry; with some systems flagged by multiple methods. We show the best-fit isochrones resulting from the CMD fits in Fig. 4. The LDB fits are shown in Fig. 6. We tabulate the best-fit values from each model and fit method in Table 1, and these are shown graphically in Fig. 7. For the Dartmouth Standard and Magnetic models, from which the lowest fit residuals for each method were derived, we assessed the concordance or internal agreement among the ages derived from the three fit methods (*Gaia*-CMD, *Gaia*-2MASS-CMD, and LDB). We performed an ANOVA analysis to assess the variance between age estimates. To do this, we computed an F-statistic as the ratio of inter-method to intra-method χ^2 . This

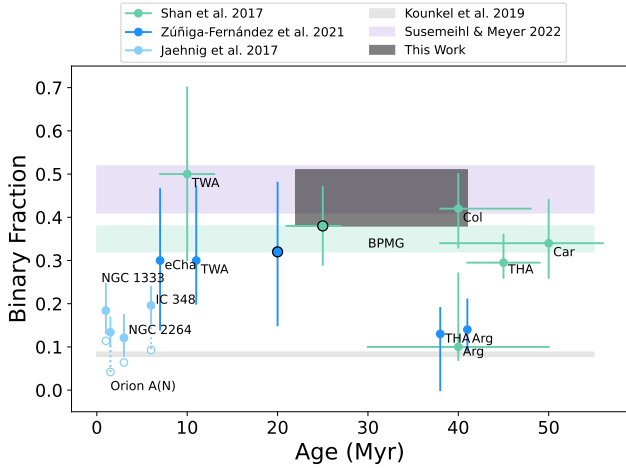


Figure 5. Binary fractions from this work compared to those from previous BPMG studies and different YMGs. Estimates for BPMG are outlined in black, and the dark grey shaded region is the result from this work. The lower bound represents the conservative binary fraction that does not include photometric binaries, and the upper bound is the fraction including photometric binaries. The Kounkel et al. (2019) (light grey shaded) region is an estimate of from RVs and the double-lined spectroscopic binary (SB2) fraction. Jaehning et al. (2017) give spectroscopic binary (SB) fractions in star-forming regions (sky blue points). The open and closed points represent the raw observed binary fractions and modeled binary fractions correcting for completeness, respectively. Shan et al. (2017) report multiplicity fractions by association (turquoise points) as well as an overall fraction (turquoise shaded region) based on AO imaging. Zúñiga-Fernández et al. (2021) also report a SB fraction (dark blue points). Susemihl & Meyer (2022) report a multiplicity fraction for M dwarfs, considering systems with mass ratios from 0.1 to 1, and separations from 0 to ∞ (purple shaded region).

analysis should be considered a rough representation of the method concordance, since we do not compute individual ages for every star, but rather a single age fit to the group locus. The measurements for each method are therefore independent of each other, and their variances cannot necessarily be compared in the way an ANOVA intends. The Dartmouth Magnetic models are the best-fitting in both the *Gaia* M_G vs. $B_P - R_P$ CMD and LDB. The method concordance ($F=0.34$; $p=0.97$; $\alpha=0.05$) suggests, however, that the internal agreement between ages is not significant, and the variance is likely attributed to the differences in the models as well as the scatter in the data. We find a similar result for the Dartmouth Standard model fits ($F=0.29$; $p=0.97$; $\alpha=0.05$).

5 DISCUSSION

We have constructed an updated catalog of the Beta Pictoris Moving Group using the most precise available photometry and astrometry and utilizing complete kinematics for membership validation. We further refined this sample by quantitatively identifying older MS interlopers aligned in kinematic space with the BPMG, but exhibiting older ages on a color-magnitude diagram. Our catalog contains a total of 106 single and resolved companions, and 47 unresolved binaries. To date, this is the most thorough vetting of stellar multiplicity in the BPMG sample, and improves upon the previous samples of Gagné & Faherty (2018) and subsequent literature by newly confirming 37 previously identified candidates and rejecting 90 others. The multiplicity fraction of $38\text{--}51\pm 7\%$ (excluding/including pho-

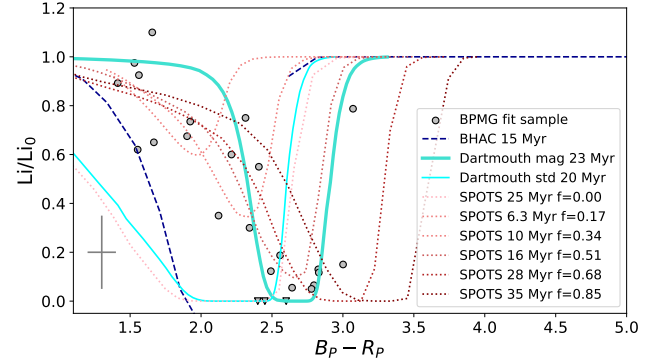


Figure 6. Li I abundances (normalized relative to an assumed primordial value $A(Li) = 3.2$) vs. *Gaia* $B_P - R_P$ color for BPMG members with 6708 Å doublet equivalent width measurements from the literature. Points plotted as triangles represent upper limits. The typical measurement uncertainty is represented as the error bar in the bottom left. For each model, the best (minimum χ^2) fit model LDB is plotted. For the incomplete LDB curves from the Baraffe et al. (2015) (BHAC) models, the fitting sample includes only those within the color ranges covered by the models.

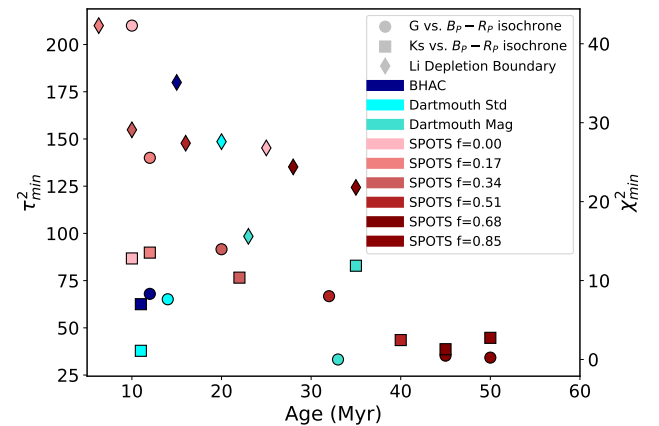


Figure 7. The results in Table 1 shown graphically. For CMD fits (circles, squares) the y-axis is τ^2 scaled on the left, while for LDB fits (diamonds), the y-axis is χ^2 scaled on the right. The two y-axis scales are not related.

tomeric binaries) reported here is in agreement with the literature (e.g., Shan et al. 2017; Zúñiga-Fernández et al. 2021) within errors (Fig. 5). The slightly higher fraction reflects improved completeness of the binary search, as previous works have tended to utilize a subset of the binary identification methods used in this work (i.e., RVs, AO imaging). The binary fractions from Kounkel et al. (2019) and Jaehning et al. (2017) in Fig. 5 are the ratio of confirmed spectroscopic binaries (SBs) to the total of their sample. Zúñiga-Fernández et al. (2021) also report SB fractions, but extrapolate to an expected occurrence rate. Since we have incompletely investigated SBs in this work (SB1s from RVs, and SB2s from literature), our multiplicity fraction is likely an underestimate.

This sample refinement appears to affect the age estimates quite variably among the different models. Curiously, with the refined single-star fit sample, one would expect the isochrone-based ages to bias older (Sullivan & Kraus 2021), but the BHAC and Dartmouth Standard models consistently produce younger ages ($\sim 11\text{--}20$ Myr) compared to the literature ($\sim 15\text{--}28$ Myr) employing the same models

(e.g., [Binks & Jeffries 2014](#); [Malo et al. 2014b](#)). One key difference between the current and previous studies is the availability of the latest *Gaia* parallaxes to compute absolute magnitudes.

Table 1. BPMG age estimates for each of the 9 evolutionary model sets and 3 age-dating methods (2 CMD and 1 LDB). The 1σ errors are given in the Age column for the best-fitting models (Dartmouth Standard and Magnetic; see Sec. 4.2). Minimum τ^2 values are given for CMD best-fit isochrones (see Sec. 3.1). Additionally, the minimum χ^2 value from the best-fit LDB ages. The best-fit age results with lowest overall residuals from each fit method (*Gaia* CMD, *Gaia*-2MASS CMD, and LDB) are boldface.

Model	Method	Age (Myr)	$\tau_{min,fit}^2 (\nu = 1)$	$\chi_{min,fit}^2 (\nu = 1)$
BHAC	<i>G</i> vs. B _P -R _P CMD	12	68.0	–
BHAC	<i>Ks</i> vs. B _P -R _P CMD	11	62.5	–
BHAC	LDB	15	–	35.1
Dartmouth Standard	<i>G</i> vs. B _P -R _P CMD	14 ⁺⁶ ₋₄	65.1	–
Dartmouth Standard	<i>Ks</i> vs. B_P-R_P CMD	11⁺⁴₋₃	37.8	–
Dartmouth Standard	LDB	20±5	–	27.6
Dartmouth Magnetic	<i>G</i> vs. B_P-R_P CMD	33⁺⁹₋₁₁	33.2	–
Dartmouth Magnetic	<i>Ks</i> vs. B _P -R _P CMD	35 ⁺¹⁰ ₋₈	82.9	–
Dartmouth Magnetic	LDB	23±8	–	15.6
SPOTS <i>f</i> =0.00	<i>G</i> vs. B _P -R _P CMD	10	210.0	–
SPOTS <i>f</i> =0.00	<i>Ks</i> vs. B _P -R _P CMD	10	86.7	–
SPOTS <i>f</i> =0.00	LDB	25	–	26.8
SPOTS <i>f</i> =0.17	<i>G</i> vs. B _P -R _P CMD	12	140.0	–
SPOTS <i>f</i> =0.17	<i>Ks</i> vs. B _P -R _P CMD	12	89.8	–
SPOTS <i>f</i> =0.17	LDB	6.3	–	42.3
SPOTS <i>f</i> =0.34	<i>G</i> vs. B _P -R _P CMD	20	91.6	–
SPOTS <i>f</i> =0.34	<i>Ks</i> vs. B _P -R _P CMD	22	76.6	–
SPOTS <i>f</i> =0.34	LDB	10	–	29.1
SPOTS <i>f</i> =0.51	<i>G</i> vs. B _P -R _P CMD	32	66.8	–
SPOTS <i>f</i> =0.51	<i>Ks</i> vs. B _P -R _P CMD	40	43.5	–
SPOTS <i>f</i> =0.51	LDB	16	–	27.4
SPOTS <i>f</i> =0.68	<i>G</i> vs. B _P -R _P CMD	45	35.3	–
SPOTS <i>f</i> =0.68	<i>Ks</i> vs. B _P -R _P CMD	45	38.7	–
SPOTS <i>f</i> =0.68	LDB	28	–	24.4
SPOTS <i>f</i> =0.85	<i>G</i> vs. B _P -R _P CMD	50	34.2	–
SPOTS <i>f</i> =0.85	<i>Ks</i> vs. B _P -R _P CMD	50	44.7	–
SPOTS <i>f</i> =0.85	LDB	35	–	28.1

There is notable internal disagreement between the models used in this study, suggesting that such age determinations are largely model- (and method-) dependent. We show in Fig. 1 the results of the present work in comparison to previous literature values. The new age estimates from the non-standard models still lie within the uncertainty spread of the literature, but tend to lie at the older end of the range. The overall best fits (by minimum τ^2 or χ^2 , producing the lowest fit residuals) from each method (the two CMDs and LDB) from the 27 estimates are in boldface in Table 1.

The model age estimate with the lowest overall residual is given by the Dartmouth magnetic models, which yield the lowest τ^2 value in a CMD. The Dartmouth magnetic models also result in the lowest fit residuals in two of the three fit methods. The Gaia G vs. $B_P - R_P$ CMD places the BPMG at 33 Myr according to the Gaia CMD, though the best-fit LDB suggests 23 Myr. We assign an uncertainty on the BPMG age due to model selection of about ± 10 Myr (see Fig. 1). The overall best-fit Gaia-2MASS isochrone is from the Dartmouth standard model and suggests a much younger age of 11 Myr, but the magnetic model returns a slightly lower τ^2 value. These two isochrone curves (Dartmouth magnetic 33 Myr and standard 11 Myr) are nearly identical, highlighted by the similarity in their offsets from the BPMG locus in the upper right panel of Fig. 4 (teal and cyan curves). The magnetic model should be more appropriate, as it should better approximate the actual physics in these highly active stars (Morris 2020).

One caveat of the isochrone fitting is that not all models are appropriate for all stars. We fit the isochrone models for BPMG members spanning a large mass range for homogeneity, however, it is expected that different models are better suited for age determination in different mass ranges. While the lower mass members should be better described by the magnetic and spot fraction models, the higher mass and hotter stars are expected to have fewer spots (Morris 2020).

In the Gaia M_G vs. $B_P - R_P$ CMD, the standard models (BHAC and Dartmouth standard) produce the shape of the BPMG locus well, but slightly overestimate the luminosity of the faintest objects. The standard models do not reproduce the shape of the LDB observed in BPMG. This, in conjunction with the poorer isochrone fits, suggests that the magnetic and spot fraction models are better suited for age-dating BPMG and similar YMGs and young associations. The 2MASS K_S vs. $B_P - R_P$ CMD generally produced poorer isochrone fits across the 9 models. And in both CMDs, the models tend to overestimate the luminosity of the bluest stars.

With increasing spot fraction, the SPOTS models tend to better fit the hottest stars while underestimating the luminosity or color of the coolest members. As mentioned in Sec. 3.1, the SPOTS models are not well calibrated in this region of the CMD (Somers et al. 2020). It is possible that the YBC-interpolated isochrones used here are neglecting to properly account for extinction and reddening, though this should not be significant for the majority of this sample. Another possibility is that the revised luminosity spot fractions (as opposed to the surface spot fraction) overestimate the true spot fractions of the low mass members, but not the higher mass members. Hence, the spot fractions should not be considered constant with stellar mass (and T_{eff}), as was assumed when the isochrones were generated. Among the SPOTS models, the overall best-performing is the $f' = 0.837$ model, which suggests an age range of 28–45 Myr. However, very high spot fractions are likely unrealistic since they have not been observed among young stars (Cao et al. 2023), and would imply lower photometric variability than observed.

Fitting to the CMD vs. the LDB returned marginally discrepant ages of 33^{+11}_{-9} and 23 ± 8 Myr, respectively. One explanation for

this divergence, compared to, e.g., the consistent CMD and LDB ages in Malo et al. (2014b), is the use of revised solar abundances from Grevesse et al. (2007) in the stellar models over previous estimates (Grevesse & Sauval 1998). It is possible that the Grevesse et al. (2007) abundances used in the current models bias CMD ages older compared to those from (Grevesse & Sauval 1998). However, the precise effects of solar abundance estimates on model ages for young stars, and which abundances are to be adopted, are yet to be determined (e.g., Asplund et al. 2021; Serenelli et al. 2009). Another explanation could be a non-solar metallicity for the BPMG, but the deployment of solar-metallicity models. Viana Almeida et al. (2009) estimated the metallicity of the BPMG as $[\text{Fe}/\text{H}] = -0.01 \pm 0.08$, but only from a single star. Preliminary tests with the Dartmouth magnetic models (G. Feiden, pers. comm.) show that a super-solar metallicity like that found in nearby young clusters (Brandt & Huang 2015; Dutra-Ferreira et al. 2016) shifts the lithium depletion pattern to higher masses, but lower T_{eff} , at a given age. This could decrease or increase the age estimate depending on the relative sampling of the warmer vs. cooler sides of the boundary (Fig. 6). These models also show that a higher metallicity produces a systematic shift to older ages in a CMD of these fully convective stars. Clearly, a robust estimate for the metallicity of the BPMG is needed and, if necessary, fitting with additional models appropriate to that value.

It is important to also consider the connections between multiplicity, rotation, and age estimates (Messina et al. 2016; Messina 2019). Tidal locking in close binaries can lead to spin-up as angular momentum is transferred from the orbit to rotation, while widely separated companions can enable spin-up by truncating and accelerating the dissipation of the circumstellar disk, halting angular momentum transfer from the star (Rosotti & Clarke 2017). Both cases lead to more rapid rotation, but past studies of the connections between binary separation, disk dissipation, and rotation have been ambiguous or contradictory (e.g., Messina et al. 2016; Allen et al. 2017; Kuruwita et al. 2018). Rotation affects the magnetic and surface activity, complicating isochrone fitting, but also affects interior mixing and lithium depletion (Somers & Pinsonneault 2015; Messina et al. 2016; Bouvier et al. 2018). Messina et al. (2016) employed the same Dartmouth models for age-dating BPMG and reported that the results significantly improve when Li EW is de-trended with rotation.

If an older age for BPMG is borne out, there are several implications for our understanding of disk and planet evolution. If the BPMG is indeed older than previously accepted, this is in agreement with the expected typical disk lifetimes of a few to tens of Myr (Richert et al. 2018), since only debris disks remain in BPMG. Additionally, any wide-orbit, directly detected substellar and planetary companions of BPMG members, e.g. 51 Eridani, and other well-studied systems mentioned in Sec. 1, would be more massive than previously determined based on their luminosity (Sullivan & Kraus 2021).

The relationship between binary separation, formation, and pre-MS evolution is not well known; this sample of young pre-MS binaries at varying separations paves the way for a detailed study of how the presence of a companion may affect pre-MS spin-down, especially since much of BPMG has been observed by continuous photometric surveys such as TESS.

6 CONCLUSIONS

In this study we presented an updated membership census and binary catalog for the Beta Pictoris Moving Group, the nearest and

youngest co-moving stellar group in the solar neighborhood. We utilized the latest and most precise space-based astrometry, photometry, and radial velocity data from *Gaia* DR3 to compute precise membership probabilities and identify binaries contaminating the samples of previous photometric age-dating studies. The *Gaia* data was supplemented with ground-based RVs from surveys and literature, and photometry from the 2MASS survey.

With the *Gaia* and RV survey data, we were able to confirm 37 new members of BPMG and reject 90 candidates (Table 3) previously identified in the literature which lacked full kinematic data. We found multiplicity fraction in the range $38\text{--}51\pm 7\%$ using multiple methods to identify resolved and unresolved binaries among the confirmed BPMG members. The single-star and resolved companion sample was used in age-dating analyses to minimize the expected age-biasing effects of unidentified binaries in a stellar sample.

We used 9 suites of evolutionary models: the BHAC standard models, Dartmouth standard and magnetic models, and the SPOTS models at 6 discrete spot fractions. We found that the difference in isochrone age between our refined sample and earlier works is smaller than the variation among isochrone ages for the different models used here. From isochrone fitting in two CMDs and from LDB fitting, we found the BPMG age ranges from 10-50 Myr. This result highlights the sensitivity of age estimates to different magnetic and spot fraction models. However, the same standard models employed in previous works still give much younger ages of 10-12 Myr, which indicates that unresolved binaries have not had a major effect on previous determinations of BPMG's age. This study shows that isochrone fitting for young stellar populations is largely sensitive to the models themselves, and that, overall, the surface spot and magnetic models out-perform the previous standards.

ACKNOWLEDGEMENTS

We thank Gary Huss for considerable and constructive feedback on earlier versions of this manuscript. R.A.L., E.G. and J. vS. are supported by NSF Astronomy & Astrophysics Research Grant 1817215. We thank the anonymous reviewer for insightful comments which have greatly improved the quality of this manuscript. This research has made use of the Keck Observatory Archive (KOA), which is operated by the W. M. Keck Observatory and the NASA Exoplanet Science Institute (NExScI), under contract with the National Aeronautics and Space Administration. This work has made use of data from the European Space Agency (ESA) mission *Gaia* (<https://www.cosmos.esa.int/gaia>), processed by the *Gaia* Data Processing and Analysis Consortium (DPAC, <https://www.cosmos.esa.int/web/gaia/dpac/consortium>). Funding for the DPAC has been provided by national institutions, in particular the institutions participating in the *Gaia* Multilateral Agreement. This publication makes use of data products from the Two Micron All Sky Survey, which is a joint project of the University of Massachusetts and the Infrared Processing and Analysis Center/California Institute of Technology, funded by the National Aeronautics and Space Administration and the National Science Foundation. Based on observations obtained at the international Gemini Observatory, a program of NSF's NOIRLab, which is managed by the Association of Universities for Research in Astronomy (AURA) under a cooperative agreement with the National Science Foundation on behalf of the Gemini Observatory partnership: the National Science Foundation (United States), National Research Council (Canada), Agencia Nacional de Investigación y Desarrollo (Chile), Ministerio de Ciencia, Tecnología e Innovación

(Argentina), Ministério da Ciência, Tecnologia, Inovações e Comunicações (Brazil), and Korea Astronomy and Space Science Institute (Republic of Korea). Based on data obtained from the ESO Science Archive Facility. This work has made use of open source Python packages NumPy (Harris et al. 2020) and SciPy (Virtanen et al. 2019).

DATA AVAILABILITY

All data used for this work are either available from the public archives (CDS) or on request from the authors. The modified SPOTS+YBC isochrones are available on Zenodo at: [LINK TO BE PROVIDED]

REFERENCES

- Allen T. S., et al., 2017, *ApJ*, **845**, 161
 Alonso-Floriano F. J., Caballero J. A., Cortés-Contreras M., Solano E., Montes D., 2015, *A&A*, **583**, A85
 Asplund M., Grevesse N., Sauval A. J., Scott P., 2009, *ARA&A*, **47**, 481
 Asplund M., Amarsi A. M., Grevesse N., 2021, *A&A*, **653**, A141
 Baraffe I., Chabrier G., Allard F., Hauschildt P. H., 1998, *A&A*, **337**, 403
 Baraffe I., Homeier D., Allard F., Chabrier G., 2015, *A&A*, **577**, A42
 Bell C. P. M., Mamajek E. E., Naylor T., 2015, *MNRAS*, **454**, 593
 Belokurov V., et al., 2020, *MNRAS*, **496**, 1922
 Binks A. S., Jeffries R. D., 2014, *MNRAS*, **438**, L11
 Binks A. S., Jeffries R. D., 2016, *MNRAS*, **455**, 3345
 Bouvier J., et al., 2018, *A&A*, **613**, A63
 Bowler B. P., et al., 2019, *ApJ*, **877**, 60
 Brandt T. D., Huang C. X., 2015, *ApJ*, **807**, 24
 Cale B. L., et al., 2021, *AJ*, **162**, 295
 Cao L., Pinsonneault M. H., van Saders J. L., 2023, *ApJ*, **951**, L49
 Chabrier G., Baraffe I., 1997, *A&A*, **327**, 1039
 Chance Q., Foreman-Mackey D., Ballard S., Casey A., David T., Price-Whelan A., 2022, arXiv e-prints, p. arXiv:2206.11275
 Chen Y., et al., 2019, *A&A*, **632**, A105
 Crundall T. D., Ireland M. J., Krumholz M. R., Federrath C., Žerjal M., Hansen J. T., 2019, arXiv e-prints, p. arXiv:1902.07732
 Dotter A., Chaboyer B., Jevremović D., Kostov V., Baron E., Ferguson J. W., 2008, *ApJS*, **178**, 89
 Duchêne G., Kraus A., 2013, *ARA&A*, **51**, 269
 Dutra-Ferreira L., Pasquini L., Smiljanic R., Porto de Mello G. F., Steffen M., 2016, *A&A*, **585**, A75
 Evans D. W., et al., 2018, *A&A*, **616**, A4
 Faherty J. K., Bochanski J. J., Gagné J., Nelson O., Coker K., Smithka I., Desir D., Vasquez C., 2018, *ApJ*, **863**, 91
 Feiden G. A., 2016, *A&A*, **593**, A99
 Feiden G. A., Chaboyer B., 2012, *ApJ*, **761**, 30
 Feiden G. A., Jones J., Chaboyer B., 2015, in 18th Cambridge Workshop on Cool Stars, Stellar Systems, and the Sun. pp 171–176 (arXiv:1408.1791)
 Fitton S., Tofflemire B. M., Kraus A. L., 2022, *Research Notes of the AAS*, **6**, 18
 Gagné J., Faherty J. K., 2018, *ApJ*, **862**, 138
 Gagné J., et al., 2018, *ApJ*, **856**, 23
 Gaia Collaboration et al., 2016, *A&A*, **595**, A1
 Gaia Collaboration et al., 2021, *A&A*, **649**, A1
 Gaidos E., et al., 2022, *MNRAS*, **514**, 1386
 Ghez A. M., McCarthy D. W., Patience J. L., Beck T. L., 1997, *ApJ*, **481**, 378
 Green G., 2018, *The Journal of Open Source Software*, **3**, 695
 Grevesse N., Sauval A. J., 1998, *Space Sci. Rev.*, **85**, 161
 Grevesse N., Asplund M., Sauval A. J., 2007, *Space Sci. Rev.*, **130**, 105
 Guiglion G., et al., 2020, *A&A*, **644**, A168

- Gustafsson B., Edvardsson B., Eriksson K., Jørgensen U. G., Nordlund Å., Plez B., 2008, *A&A*, **486**, 951
- Harris C. R., et al., 2020, *Nature*, **585**, 357
- Higashio S., et al., 2022, *ApJ*, **933**, 13
- Hodapp K. W., et al., 2003, *PASP*, **115**, 1388
- Jaehnig K., Bird J. C., Stassun K. G., Da Rio N., Tan J. C., Cotaar M., Somers G., 2017, *ApJ*, **851**, 14
- Kalasz P., Liu M. C., Matthews B. C., 2004, *Science*, **303**, 1990
- Kastner J. H., Principe D. A., 2022, arXiv e-prints, p. [arXiv:2204.00863](https://arxiv.org/abs/2204.00863)
- Kiss L. L., et al., 2011, *MNRAS*, **411**, 117
- Kounkel M., et al., 2019, *AJ*, **157**, 196
- Kraus A. L., Hillenbrand L. A., 2008, *ApJ*, **686**, L111
- Krumholz M. R., McKee C. F., Bland-Hawthorn J., 2019, *ARA&A*, **57**, 227
- Kuruwita R. L., Ireland M., Rizzuto A., Bento J., Federrath C., 2018, *MNRAS*, **480**, 5099
- Lagrange A. M., et al., 2010, *Science*, **329**, 57
- Lagrange A. M., et al., 2020, *A&A*, **642**, A18
- Lecavelier Des Etangs A., et al., 1993, *A&A*, **274**, 877
- Lee J., Song I., 2018, *MNRAS*, **475**, 2955
- Lee J., Song I., Murphy S. J., 2022, *MNRAS*, **511**, 6179
- Leike R. H., Glatzle M., Enßlin T. A., 2020, *A&A*, **639**, A138
- Lenzen R., et al., 2003, in Iye M., Moorwood A. F. M., eds, Society of Photo-Optical Instrumentation Engineers (SPIE) Conference Series Vol. 4841, Instrument Design and Performance for Optical/Infrared Ground-based Telescopes. pp 944–952, doi:[10.1117/12.460044](https://doi.org/10.1117/12.460044)
- Liu M. C., et al., 2013, *ApJ*, **777**, L20
- Macintosh B., et al., 2015, *Science*, **350**, 64
- Malo L., Artigau É., Doyon R., Lafrenière D., Albert L., Gagné J., 2014a, *ApJ*, **788**, 81
- Malo L., Doyon R., Feiden G. A., Albert L., Lafrenière D., Artigau É., Gagné J., Riedel A., 2014b, *ApJ*, **792**, 37
- Mamajek E. E., Bell C. P. M., 2014, *MNRAS*, **445**, 2169
- Mentuch E., Brandeker A., van Kerkwijk M. H., Jayawardhana R., Hauschildt P. H., 2008, *ApJ*, **689**, 1127
- Messina S., 2019, *A&A*, **627**, A97
- Messina S., Leto G., Pagano I., 2016, *Ap&SS*, **361**, 291
- Messina S., et al., 2017, preprint, ([arXiv:1707.01682](https://arxiv.org/abs/1707.01682))
- Miret-Roig N., et al., 2020, *A&A*, **642**, A179
- Morris B. M., 2020, *ApJ*, **893**, 67
- Naylor T., Jeffries R. D., 2006, *MNRAS*, **373**, 1251
- Nielsen E. L., et al., 2019, *AJ*, **158**, 13
- Palla F., Randich S., Pavlenko Y. V., Flaccomio E., Pallavicini R., 2007, *ApJ*, **659**, L41
- Pecaut M. J., Mamajek E. E., 2013, *ApJS*, **208**, 9
- Pecaut M. J., Mamajek E. E., 2016, *MNRAS*, **461**, 794
- Pedregosa F., et al., 2011, *Journal of Machine Learning Research*, **12**, 2825
- Plavchan P., et al., 2020, *Nature*, **582**, 497
- Richert A. J. W., Getman K. V., Feigelson E. D., Kuhn M. A., Broos P. S., Povich M. S., Bate M. R., Garmire G. P., 2018, *MNRAS*, **477**, 5191
- Rosotti G. P., Clarke C. J., 2017, preprint, ([arXiv:1710.08920](https://arxiv.org/abs/1710.08920))
- Rousset G., et al., 2003, in Wizinowich P. L., Bonaccini D., eds, Society of Photo-Optical Instrumentation Engineers (SPIE) Conference Series Vol. 4839, Adaptive Optical System Technologies II. pp 140–149, doi:[10.1117/12.459332](https://doi.org/10.1117/12.459332)
- Schneider A. C., Shkolnik E. L., Allers K. N., Kraus A. L., Liu M. C., Weinberger A. J., Flagg L., 2019, *AJ*, **157**, 234
- Serenelli A. M., Basu S., Ferguson J. W., Asplund M., 2009, *ApJ*, **705**, L123
- Service M., Lu J. R., Campbell R., Sitarski B. N., Ghez A. M., Anderson J., 2016, *PASP*, **128**, 095004
- Shan Y., et al., 2017, *ApJ*, **846**, 93
- Shkolnik E. L., Allers K. N., Kraus A. L., Liu M. C., Flagg L., 2017, *AJ*, **154**, 69
- Silverberg S. M., et al., 2020, *ApJ*, **890**, 106
- Skrutskie M. F., et al., 2006, *AJ*, **131**, 1163
- Soderblom D. R., Jones B. F., Balachandran S., Stauffer J. R., Duncan D. K., Fedele S. B., Hudon J. D., 1993, *AJ*, **106**, 1059
- Somers G., Pinsonneault M. H., 2015, *Monthly Notices of the Royal Astronomical Society*, **449**, 4131
- Somers G., Cao L., Pinsonneault M. H., 2020, *ApJ*, **891**, 29
- Steinmetz M., et al., 2020, *AJ*, **160**, 82
- Sullivan K., Kraus A. L., 2021, *ApJ*, **912**, 137
- Susemihl N., Meyer M. R., 2022, *A&A*, **657**, A48
- Terrien R. C., Mahadevan S., Deshpande R., Bender C. F., 2015, *ApJS*, **220**, 16
- Ujjwal K., Kartha S. S., Mathew B., Manoj P., Narang M., 2020, *AJ*, **159**, 166
- Viana Almeida P., Santos N. C., Melo C., Ammler-von Eiff M., Torres C. A. O., Quast G. R., Gameiro J. F., Sterzik M., 2009, *A&A*, **501**, 965
- Virtanen P., et al., 2019, arXiv e-prints, p. [arXiv:1907.10121](https://arxiv.org/abs/1907.10121)
- Winters J. G., et al., 2019, *AJ*, **157**, 216
- Wood M. L., Mann A. W., Kraus A. L., 2021, *AJ*, **162**, 128
- Ziegler C., et al., 2018, *AJ*, **156**, 83
- Zúñiga-Fernández S., et al., 2020, arXiv e-prints, p. [arXiv:2010.08575](https://arxiv.org/abs/2010.08575)
- Zúñiga-Fernández S., et al., 2021, *A&A*, **645**, A30
- Zuckerman B., Song I., Bessell M. S., Webb R. A., 2001, *ApJ*, **562**, L87

APPENDIX A:

We list the confirmed BPMG members and their binary designation in Table 2, and provide a list of rejected candidates in Table 3.

Table 2. Confirmed members of the Beta Pictoris Moving Group¹

<i>Gaia</i> DR3 ID	2MASS ID	Common Name	RA (hh:mm:ss.ss)	Dec (dd:mm:ss.s)	π (mas)	<i>Gaia</i> <i>G</i>	$B_p - R_p$	Binary ²	Separation (\prime) ³
2315841869173294208	00275035-3233238	GJ 2006 B	00:27:50.35	-32:33:24.13	28.59	11.92	2.80	R	17.890
2315849737553379840	00281434-3227556	GR* 9	00:28:14.35	-32:27:55.62	28.56	13.44	3.31	N	
2357025657739386624	00482667-1847204		00:48:26.67	-18:47:20.42	19.42	13.94	3.16	N	
2581708281894978176	00501752+0837341		00:50:17.51	+08:37:34.20	6.31	12.85	3.00	U	
2788357364871430400	01025097+1856543		01:02:50.99	+18:56:54.16	26.19	12.58	2.95	U	
2477870708709917568	01351393-0712517	Barta 161 12	01:35:13.92	-07:12:51.46	26.82	11.97	2.83	U	
73034991155555456	02175601+1225266		02:17:56.02	+12:25:26.42	15.90	12.81	2.64	U	
87555176071871744	02241739+2031513		02:24:17.40	+20:31:51.42	14.13	16.04	3.67	N	
132363027978672000	02272804+3058405	AG Tri B	02:27:28.06	+30:58:40.36	24.43	11.43	2.41	R	22.050
132362959259196032	02272924+3058246	AG Tri A	02:27:29.25	+30:58:24.60	24.42	9.74	1.55	U	
22338644598132096	02442137+1057411	MCC 401	02:44:21.37	+10:57:41.07	20.78	10.33	1.95	R	0.223
5177677603263978880	02450826-0708120		02:45:08.27	-07:08:12.09	14.66	14.00	3.11	N	
5183875103632956032	02495639-0557352		02:49:56.38	-05:57:35.43	15.09	15.66	3.88	U	
68012529415816832	03350208+2342356	EPIC 211046195	03:35:02.09	+23:42:35.41	19.72	16.30	4.50	N	
244734765608363136	03393700+4531160		03:39:37.01	+45:31:15.97	24.82	12.89	2.85	U	
66245408072670336	03573393+2445106	StKM 1-433	03:57:33.93	+24:45:10.64	14.55	11.86	1.98	N	
3205094369407459456	04373746-0229282	GJ 3305	04:37:37.46	-02:29:28.95	36.01	9.80	2.12	R	0.235
175329120598595200	04435686+3723033	PM J04439+3723W	04:43:56.87	+37:23:03.36	14.01	12.31	2.34	R	7.650
3231945508509506176	04593483+0147007	V1005 Ori	04:59:34.83	+01:47:00.67	40.99	9.32	1.90	N	
4764027962957023104	05004714-5715255	CD-57 1054	05:00:47.13	-57:15:25.45	37.21	9.38	1.92	N	
3228854506445679616	05015665+0108429		05:01:56.65	+01:08:42.90	39.54	11.51	2.86	U	
3238965099979863296	05061292+0439272		05:06:12.93	+04:39:27.18	36.19	11.99	2.93	N	
2962658549474035584	05064991-2135091	BD-21 1074 A	05:06:49.50	-21:35:04.30	50.43	9.56	2.24	R	7.790
2901786974419551488	05294468-3239141	SCR J0529-3239	05:29:44.69	-32:39:14.30	33.60	12.27	3.03	N	
3216729573251961856	05320450-0305291	V* V1311 Ori	05:32:04.50	-03:05:29.40	27.22	10.44	2.27	R	0.159
3216922640621225088	05335981-0221325		05:33:59.82	-02:21:32.38	29.12	11.27	2.49	U	
2899492637251200512	06131330-2742054		06:13:13.32	-27:42:05.57	29.62	10.94	2.74	R	0.110
5266270443442455040	06182824-7202416	AO Men	06:18:28.21	-72:02:41.45	25.57	9.27	1.41	N	
5412403269717562240	09462782-4457408		09:46:27.82	-44:57:40.85	21.44	14.52	3.71	N	
5355751581627180288	10172689-5354265	TWA 22 A	10:17:26.89	-53:54:26.39	50.52	12.06	3.53	R	0.106
5849837854861497856	14423039-6458305	* alf Cir	14:42:30.42	-64:58:30.49	60.99	3.17	0.54	U	
5882581895192805632	15385679-5742190	V343 Nor BC	15:38:56.78	-57:42:18.95	25.44	13.21	3.03	R	10.450
5882581895219921024	15385757-5742273	V343 Nor A	15:38:57.56	-57:42:27.35	25.83	7.68	1.00	U	
5935776714456619008	16572029-5343316		16:57:20.27	-53:43:31.58	19.69	11.35	2.43	R	0.100
5963633872326630272	17024014-4521587	UCAC2 12510535	17:02:40.16	-45:21:58.72	31.30	10.70	2.29	N	
4107812485571331328	17150362-2749397	CD-27 11535	17:15:03.61	-27:49:39.74	12.00	10.09	1.56	R	0.141
5811866422581688320	17172550-6657039	HD 155555 B	17:17:25.51	-66:57:03.73	32.95	6.46	1.00	U	
5811866422581688320	17172550-6657039	HD 155555 A	17:17:25.51	-66:57:03.73	32.95	6.46	1.00	U	
5811866358170877184	17173128-6657055	HD 155555 C	17:17:31.29	-66:57:05.47	32.88	11.47	2.73	R	34.010
5924485966955008896	17295506-5415487	CD-54 7336	17:29:55.08	-54:15:48.65	14.79	9.32	1.08	N	
4067828843907821824	17520173-2357571	UCAC4 331-124196	17:52:01.74	-23:57:57.22	15.67	11.85	2.21	N	
4050178830427649024	18041617-3018280		18:04:16.18	-30:18:27.96	18.15	11.74	2.33	N	

¹The extended machine-readable catalog is available by request. ²N = not binary, U = unresolved binary, and R = resolved binary. ³For wide binaries or those resolved by *Gaia* or AO.

Table 2, continued.

<i>Gaia</i> DR3 ID	2MASS ID	Common Name	RA (hh:mm:ss.ss)	Dec (dd:mm:ss.s)	π (mas)	<i>Gaia</i> <i>G</i>	$B_P - R_P$	Binary ²	Separation (\prime) ³
6648834361774839040	18055491-5704307	UCAC3 66-407600	18:05:54.92	-57:04:30.74	17.71	12.36	2.62	N	
6414282147589248000	18090694-7613239		18:09:06.93	-76:13:23.89	36.66	13.26	3.42	N	
6653162456161626368	18092970-5430532		18:09:29.71	-54:30:53.27	25.67	13.34	3.39	U	
4045698732855626624	18142207-3246100		18:14:22.07	-32:46:10.13	13.92	11.91	2.17	R	1.200
6706431763001502848	18151564-4927472		18:15:15.64	-49:27:47.30	16.13	11.70	2.53	U	
4051081838710783232	18195221-2916327	HD 168210	18:19:52.21	-29:16:32.82	12.43	8.67	0.92	U	
6705107126367751168	18265401-4807022	HD 169405	18:26:54.01	-48:07:02.06	12.20	5.22	1.03	U	
6723183789033085824	18283208-4129081	TYC 7909-2501-1	18:28:32.09	-41:29:08.36	14.96	10.86	1.63	U	
6649786646225001984	18420483-5554126		18:42:04.84	-55:54:12.74	19.36	13.84	3.08	N	
6649788119394186112	18420694-5554254		18:42:06.96	-55:54:25.58	19.44	12.33	2.64	N	
6728469996119674112	18430597-4058047		18:43:05.97	-40:58:04.78	17.10	12.10	2.50	U	
6650036304082834560	18443965-5506502		18:44:39.66	-55:06:50.09	11.02	10.24	1.36	U	
6631685008336771072	18465255-6210366	Smethells 20	18:46:52.55	-62:10:36.61	19.72	11.13	2.05	N	
4071532308311834496	18471351-2808558		18:47:13.51	-28:08:55.86	16.69	15.25	3.54	N	
6736232346363422336	18504448-3147472	CD-31 16041	18:50:44.48	-31:47:47.38	20.22	10.49	1.82	N	
6655168686921108864	18530587-5010499	HIP 92680	18:53:05.87	-50:10:49.90	21.16	8.10	0.97	N	
4088823159447848064	19082195-1603249		19:08:21.96	-16:03:24.82	14.35	15.77	3.69	U	
6764026419748892160	19114467-2604085	CD-26 13904	19:11:44.67	-26:04:08.53	14.77	9.88	1.40	R	0.210
6663346029775435264	19233820-4606316		19:23:38.21	-46:06:31.64	14.03	11.21	1.79	N	
6742986538895222144	19243494-3442392		19:24:34.95	-34:42:39.37	19.40	12.77	2.99	U	
6643851448094862592	19260075-5331269		19:26:00.75	-53:31:26.97	20.94	12.57	2.91	U	
6764421281858414208	19300396-2939322		19:30:03.96	-29:39:32.45	16.60	13.20	2.91	N	
6754492966739292928	19481651-2720319		19:48:16.52	-27:20:31.94	15.47	12.21	2.29	N	
6754492932379552896	19481703-2720334		19:48:17.05	-27:20:33.50	15.34	17.16	3.93	N	
6747467431032539008	19560294-3207186		19:56:02.94	-32:07:18.66	19.54	11.91	2.78	R	26.310
6747467224874108288	19560438-3207376	TYC 7443-1102-1	19:56:04.37	-32:07:37.67	19.49	10.83	1.86	N	
6747106443324127488	20013718-3313139		20:01:37.17	-33:13:14.01	16.68	11.46	2.07	N	
6700649538727351040	20055640-3216591		20:05:56.41	-32:16:59.19	20.18	11.20	2.08	N	
6850555648387276544	20083784-2545256		20:08:37.85	-25:45:25.71	17.85	14.15	3.18	N	
6800238044930953600	20333759-2556521		20:33:37.60	-25:56:52.12	22.90	13.08	3.36	U	
6794047652729201024	20450949-3120266	AU Mic	20:45:09.53	-31:20:27.24	102.94	7.84	2.11	N	
6833291426043854976	21100461-1920302		21:10:04.61	-19:20:30.44	29.77	11.62	3.05	R	0.141
6833292181958100224	21100535-1919573		21:10:05.36	-19:19:57.61	30.90	10.81	2.42	N	
6801191424589717888	21103096-2710513	BRG 32B	21:10:30.97	-27:10:51.53	24.84	14.85	3.75	N	
6801191355870240768	21103147-2710578		21:10:31.48	-27:10:58.01	24.76	13.58	3.28	N	
6835588645136005504	21200779-1645475		21:20:07.81	-16:45:47.80	20.72	13.14	2.88	N	
6400160947954197888	21212873-6655063		21:21:28.72	-66:55:06.27	31.70	9.99	1.84	U	
2727844441062478464	22085034+1144131		22:08:50.34	+11:44:13.22	26.75	13.02	3.06	U	
6608255235884536320	22334687-2950101		22:33:46.89	-29:50:10.22	19.19	16.89	4.41	N	
6382640367603744128	22424896-7142211		22:42:48.93	-71:42:21.20	27.23	9.82	1.75	N	
6603693881832177792	22445794-3315015	HIP 112312 A	22:44:57.96	-33:15:01.74	47.92	10.74	2.78	R	35.880
6603693808817829760	22450004-3315258	HIP 112312 B	22:45:00.06	-33:15:26.09	48.00	11.82	3.07	N	
2433191886212246784	23323085-1215513	BD-13 6424	23:32:30.86	-12:15:51.46	36.43	9.83	2.03	N	
2324205785406060928	23355015-3401477		23:35:50.17	-34:01:47.78	26.76	15.29	3.82	N	

¹The extended machine-readable catalog is available by request. ²N = not binary, U = unresolved binary, and R = resolved binary. ³For wide binaries or those resolved by *Gaia* or AO.

This paper has been typeset from a \TeX/L\AA\TeX file prepared by the author.

Table 3. Rejected Beta Pictoris Moving Group candidates. The probability of membership to BPMG based on proper motions, parallax, and RV is listed in column $\log P_{BPMG}$.

Gaia DR3 ID	2MASS ID	Common Name	RA (hh:mm:ss.ss)	Dec (dd:mm:ss.s)	$\log P_{BPMG}$
6882840883190250752	20554767-1706509	HIP 103311 AB	20 55 47.74	-17 06 51.97	-999
1227780314970612864	14255593+1412101	J1425+1412	14 25 55.87	+14 12 09.64	-999
4707563810327288192	00172353-6645124	RBS 38	00 17 23.81	-66 45 12.59	-999
4630867449747185280	00181936-8207151	2MASS J00181936-8207151	00 18 25.97	-82 07 14.44	-999
5505087564445324160	07063751-4943243	J0706-4943	07 06 37.46	-49 43 23.66	-999
2749470902772705408	00323480+0729271	J0032+0729	00 32 34.91	+07 29 25.78	-210.166853
6656461918753123968	19063412-5327481	J1906-5327	19 06 34.15	-53 27 49.09	-168.301030
81166811651514880	02355424+1514561	TYC 1216-1411-1	02 35 54.31	+15 14 54.97	-154.970616
2683714304930755712	22064638+0325037	Wolf 990	22 06 46.85	+03 24 58.90	-110.518557
2306957128025970944	00042123-3733083	2MASS J00042123-3733083	00 04 21.60	-37 33 10.77	-96.376751
3292922293081928192	04484752+0940281	HD 287167	04 48 47.55	+09 40 27.49	-90.142668
4805600119646735616	05332802-4257205	RBS 661	05 33 28.01	-42 57 19.94	-82.000435
109628013733250304	02515408+2227299	2MASS J02515408+2227299	02 51 54.22	+22 27 28.22	-51.667562
126534203306473344	02383622+2614198	BD+25 430	02 38 36.29	+26 14 18.97	-43.732828
6652273015676968832	18103569-5513435	J1810-5513	18 10 35.72	-55 13 45.00	-40.366532
1704563363189801600	16171135+7733477	J1617+7733	16 17 11.21	+77 33 48.33	-38.022734
1066495290754663040	10015995+6651278	J1001+6651	10 01 59.75	+66 51 26.43	-34.082494
3899393459350372224	11515681+0731262	J1151+0731	11 51 56.69	+07 31 25.26	-33.636388
5055946513425551360	03370343-3042318	J0337-3042	03 37 03.47	-30 42 32.01	-25.756962
5209118305765620096	08475676-7854532	V* EQ Cha	08 47 56.60	-78 54 52.78	-25.747147
4988735051246293504	01132817-3821024	J0113-3821	01 13 28.31	-38 21 03.73	-25.256490
6718463138927725696	19033299-3847058	2MASS J19033299-3847058	19 03 33.04	-38 47 07.85	-20.779892
4860805567684944128	03255277-3601161	J0325-3601	03 25 52.82	-36 01 16.23	-20.508638
5132219016567875200	02335984-1811525	BRG 13	02 33 59.9	-18 11 52.99	-20.089376
1725580076982641280	14124993+8401311	J1412+8401	14 12 49.47	+84 01 31.83	-19.049149
4980384088633481216	00325584-4405058	J0032-4405	00 32 56.03	-44 05 07.26	-18.756962
4093006560668685568	18235116-1930168	HD 313300	18 23 51.21	-19 30 17.49	-15.991400
6200370648577945216	15063505-3639297	J1506-3639	15 06 35.02	-36 39 30.16	-15.818156
5050451154310013056	02505959-3409050	J0250-3409	02 50 59.73	-34 09 05.50	-15.782516
1930104018733997312	23010610+4002360	J2301+4002	23 01 06.20	+40 02 35.79	-15.059982
2517397846786452224	02261625+0617331	HD 15115	02 26 16.34	+06 17 32.41	-14.882729
6701528082880793088	18091388-5302176	J1809-5302	18 09 13.87	-53 02 18.38	-14.785156
4721078629298085760	02564708-6343027	J0256-6343	02 56 47.23	-63 43 02.57	-14.249492
5200035927402217088	11493184-7851011	V* DZ Cha	11 49 31.63	-78 51 01.12	-13.725842
5084713036143375744	03363144-2619578	J0336-2619	03 36 31.55	-26 19 58.34	-13.353596
3920498104009539456	12115308+1249135	J1211+1249	12 11 53.01	+12 49 13.02	-12.404504
4946632929953255040	02304623-4343493	UCAC4 232-002301	02 30 46.36	-43 43 49.74	-12.164944
735219962087569792	10355725+2853316	J1035+2853	10 35 57.13	+28 53 30.38	-12.152427
4920330653311504256	00413538-5621127	J0041-5621	00 41 35.60	-56 21 13.79	-12.063486
3193496682100879872	03550477-1032415	J0355-1032	03 55 04.85	-10 32 42.13	-11.596879
5050649616159457280	02485260-3404246	J0248-3404 AB	02 48 52.73	-34 04 25.10	-11.301030
1747664867537511424	20395460+0620118	BD+05 4576	20 39 54.70	+06 20 10.27	-11.253366
1851787179879007232	21183375+3014346	TYC 2703-706-1	21 18 33.83	+30 14 34.27	-11.195861
2851052759133803776	23512227+2344207	J2351+2344	23 51 22.60	+23 44 19.37	-10.939302
6772888139870271744	19312434-2134226	J1931-2134	19 31 24.40	-21 34 24.43	-10.575118
5314991556010305024	08412528-5736021	J0841-5736	08 41 25.25	-57 36 02.48	-10.126098
3339914973377653760	05363846+1117487	J0536+1117	05 36 38.46	+11 17 47.84	-10.082494
2430275225461072128	00274534-0806046	J0027-0806	00 27 45.47	-08 06 05.62	-9.931814
4131758504393326592	16430128-1754274	J1643-1754	16 43 01.26	-17 54 28.32	-9.657577
4931155036049677312	01372781-4558261	2MASS J01372781-4558261	01 37 28.0	-45 58 26.76	-9.046240
5250988846733325312	09315840-6209258	J0931-6209	09 31 58.33	-62 09 25.46	-8.982967
3240921406042422400	05200029+0613036	THOR 11	05 20 00.31	+06 13 03.18	-8.062984
6730618549223057664	18435838-3559096	J1843-3559	18 43 58.39	-35 59 10.10	-7.974694
6668403989418902144	20320890-4742064	HD 195266	20 32 09.01	-47 42 08.64	-7.872895
527849041138749056	00270283+6630389	J0027+6630	00 27 03.02	+66 30 38.62	-7.723538
599277851962810112	08224748+0757171	J0822+0757	08 22 47.45	+07 57 16.26	-7.625252
628827128175694976	10141918+2104297	MCC 124	10 14 19.03	+21 04 26.85	-7.252588
602637929434290304	08290411+1125053	J0829+1125	08 29 04.06	+11 25 04.31	-7.139063
3240923360251087104	05203182+0616115	THOR 10	05 20 31.83	+06 16 11.08	-7.116907
4745195905754074496	02365171-5203036	J0236-5203	02 36 51.87	-52 03 03.61	-6.761954
2854508592899528192	23500639+2659519	J2350+2659	23 50 06.62	+26 59 51.20	-6.458421
288290097672550528	01303534+2008393	J0130+2008	01 30 35.42	+20 08 38.82	-5.804100

Table 3, continued.

<i>Gaia</i> DR3 ID	2MASS ID	Common Name	RA (hh:mm:ss.ss)	Dec (dd:mm:ss.s)	log <i>P_{BPMG}</i>
1915678735414682368	22571130+3639451	J2257+3639	22 57 11.38	+36 39 44.95	-5.576754
3209947441933983744	05204041-0547109	BD-05 1229	05 20 40.42	-05 47 11.65	-4.692504
18211043587721088	02412589+0559181	BD+05 378	02 41 25.97	+05 59 17.52	-4.457175
3002957677856537728	06322029-0943290	UCAC4 402-013866	06 32 20.28	-09 43 29.85	-3.610379
2797571482766220160	00193931+1951050	2MASS J00193931+1951050	00 19 39.4	+19 51 04.37	-3.456861
59000206263788672	03105356+1838385	J0310+1838	03 10 53.63	+18 38 37.53	-3.308083
4482593565100321664	18011345+0948379	J1801+0948	18 01 13.44	+09 48 37.36	-2.343479
2962658549474035712	05064946-2135038	BD-21 1074 B	05 06 49.48	-21 35 04.27	-2.284901
898486306258888832	07293108+3556003	J0729+3556	07 29 31.04	+35 55 58.60	-2.265637
6104139604209342464	14252913-4113323	UCAC3 98-153320	14 25 29.06	-41 13 33.05	-2.254027
5226193446465971072	11091606-7352465	J1109-7352	11 09 15.86	-73 52 46.38	-2.161118
2797571448406493056	00194303+1951117	J0019+1951	00 19 43.12	+19 51 11.07	-2.156805
4154524481067422976	18202275-1011131	J1820-1011	18 20 22.74	-10 11 14.07	-2.074230
3306841457454198016	04232720+1115174	J0423+1115	04 23 27.23	+11 15 16.84	-1.706733
3623343812312995584	13215631-1052098	J1321-1052	13 21 56.25	-10 52 10.79	-1.705694
4946633857666189952	02303239-4342232	CD-44 753	02 30 32.42	-43 42 23.39	-1.584435
2556724418479276416	00464841+0715177	J0046+0715	00 46 48.52	+07 15 16.82	-1.575535
3996306127913903232	10593834+2526155	BD+26 2161	10 59 38.11	+25 26 14.69	-0.896972
3181961503752885248	05063003-1102350	HD 32965	05 06 30.08	-11 02 35.83	-0.701318
132592688469662208	02224082+3055161	J0222+3055	02 22 40.93	+30 55 15.0	-0.585495
1905055700744817024	22184265+3321137	J2218+3321	22 18 42.73	+33 21 13.45	-0.472521
6760846563417053056	18580415-2953045	J1858-2953	18 58 04.17	-29 53 05.42	-0.455103
2640348977921037056	23314492-0244395	AF Psc	23 31 45.02	-02 44 40.66	-0.242801
2507726817386336512	01561492+0006088	UCAC4 451-002420	01 56 15.04	+00 06 07.81	-0.157852
2315841869173294080	00275023-3233060	GJ 2006 A	00 27 50.37	-32 33 07.04	-0.147485
6633474669669267712	19010683-5853301	HD 175897	19 01 6.86	-58 53 30.88	-0.103548
2962794236080240128	05082729-2101444	J0508-2101	05 08 27.33	-21 01 44.57	-0.094709
799092516692729344	09361593+3731456	J0936+3731	09 36 15.78	+37 31 44.12	-0.062335